Role of Sulfur Vacancies and Undercoordinated Mo Regions in MoS 2 Nanosheets toward the Evolution of Hydrogen

Lei Li, Zhaodan Qin, Lucie Ries, Song Hong, Thierry Michel, Jieun Yang, Chrystelle Salameh, Mikhael Bechelany, Philippe Miele, Daniel Kaplan, et al.

Role of Sulfur Vacancies and Undercoordinated Mo Regions in MoS_2 Nanosheets Towards the Evolution of Hydrogen

Lei Li,[1,2] Zhaodan Qin,[1] Lucie Ries,[1] Song Hong,[3] Thierry Michel,[4] Jieun Yang,[5] Chrystelle Salameh,[1] Mikhael Bechelany,[1] Philippe Miele,[1,6] Daniel Kaplan,[7] Manish Chhowalla,[5] Damien Voiry[1,*]

[1]*Institut Européen des Membranes, IEM, UMR 5635, Université Montpellier, ENSCM, CNRS, 34095 Montpellier Cedex5, France*

[2]*College of Biological, Chemical Sciences and Engineering, Jiaxing University, Jiaxing, Zhejiang 314001, China*

[3]*College of Materials Science and Engineering, Beijing University of Chemical Technology, Beijing 100029, China*

[4]*Laboratoire Charles Coulomb, L2C, Université de Montpellier, CNRS, 34095 Montpellier, France.*

[5]*Materials Science and Engineering, Rutgers University, 607 Taylor Road, Piscataway, New Jersey 08854, USA*

[6]*Institut Universitaire de France (IUF), MESRI, 1 rue Descartes, 75231 Paris cedex 05, France.*

[7]*US Army RDECOM-ARDEC, Advanced Materials Technology Branch, Picatinny Arsenal, New Jersey 07806, USA.*

*Correspondence to: damien.voiry@umontpellier.fr

ABSTRACT

Low dimensional materials have been examined as electrocatalysts for the hydrogen evolution reaction (HER). Among them, two-dimensional Transition Metal Dichalcogenides (2D-TMDs) such as MoS_2 have been identified as potential candidates. However, the performance of TMDs towards HER in both acidic and basic media remains inferior to that of noble metals such as Pt and its alloys. This calls for investigating the influence of controlled defect engineering of 2D

TMDs on their performance towards hydrogen production. Here we explored the HER activity from defective multilayered MoS_2 over a large range of surface S vacancy concentrations up to 90%. Amorphous MoS_2 and 2H MoS_2 with ultra-rich S vacancies demonstrated the highest HER performance in acid and basic electrolyte respectively. We also report that the HER performance from multilayered MoS_2 can be divided into two domains corresponding to "point defects" at low concentrations of surface S vacancies (Stage 1) and large regions of undercoordinated Mo atoms for high concentrations of surface S vacancies (Stage 2). The highest performance is obtained for Stage 2 in the presence of undercoordinated Mo atoms with a TOF of ~ 2 s^{-1} at an overpotential of 160 mV in 0.1 M KOH which compares favorably to the best results in the literature. Overall our work provides deeper insight on the HER mechanism from defected MoS_2 and provides guidance for the development of defect-engineered TMD-based electrocatalysts.

KEYWORDS

hydrogen evolution reaction, MoS_2, sulfur vacancies, undercoordinated Mo, H_2-annealing

The emergence of systems able to convert or to store energy requires the development of smart materials that are more efficient and stable, and ideally made of earth abundant elements. Many of these systems operate *via* electrochemical reactions: fuel cells,[1] batteries[2] and electrolyzers.[3,4] Two-dimensional (2D) materials have emerged as a fascinating class of electrocatalytic materials demonstrating excellent activity for key electrochemical processes including the hydrogen evolution reaction (HER),[5-10] the oxygen evolution reaction (OER)[11,12] and the CO_2 reduction reaction (CO_2RR).[13-16] HER is indeed one of the most promising reactions for the production of hydrogen (H_2) from water. In order to find alternatives to expensive and

scarce noble metals, 2D electrocatalysts based on earth abundant elements are currently being investigated among other candidates based on metal carbides,[17-19] metal nitrides,[20-22] metal phosphides[23,24] or metal sulfide nanoparticles.[25-32] Transition metal dichalcogenides (TMDs) have shown promise towards the evolution of hydrogen since the seminal work from Hinnemann *et al*.[33] The main proposed strategies include *i*) the maximization of the density of active sites, *ii*) the improvement of the reaction kinetics *via* the reduction of the charge transfer resistance and *iii*) the optimization of the intrinsic activity of the TMD nanosheets. For instance, the charge transfer resistance can be reduced through modifying the electronic properties using elemental doping (*e.g.*, N, P)[34] of TMDs or of the conductive supports (*e.g.*, N-doped porous carbon).[35,36] Moreover doping with nitrogen, boron or phosphorus has also been identified as an efficient lever to optimize the electrocatalytic properties *via* the modification of the free energy of adsorption of the reactant and the intermediate species.[37-39] Similarly the optimization of the intrinsic activity of TMDs has notably led to the exploration of methods for activating the active sites *via* phase,[40,41] defect and strain engineering.[42-48] We have previously reported that the metallic 1T phase of TMDs can enhance the activity by activating the basal plane and improving the injection of electrons into the MoS_2 nanosheets.[40,49] Alternatively, Xie's group first identified the beneficial role of defects in MoS_2 slabs on HER activity.[50] Since then, several strategies for defect engineering have been reported based on controlled hydrothermal growth,[51] plasma,[52,53] electrochemical desulfurization[54] and chemical treatments.[55] Defects in the form of sulfur (S) vacancies are expected to induce a reduction of the free energy of hydrogen adsorption: ΔG_{H^*} on the basal planes of the MoS_2 nanosheets.[53] However, these predictions of the HER performance have been performed assuming point-defect S-vacancies whereas the influence of point defects *versus* undercoordinated Mo remains unclear. Experimentally, the effect of sulfur vacancies has

been explored from 0% up ~ 15 % in acid conditions,[43-45, 50-55] while the behavior of defected MoS_2 in alkaline medium is less explored. For instance, recent results from the Lewis group have proposed that – contrary to the situation in acidic media where the edges are active – in basic media, the terraces are involved in the HER mechanism.[56]

The development of optimized HER electrocatalysts based on engineered TMDs calls for painstaking exploration of the reaction mechanisms on defected MoS_2. Here, we report a detailed study of the influence of the crystallinity as well as the concentration of surface S-vacancies in multilayered MoS_2 on the HER activity in both acidic and basic electrolytes. The combination of physical characterization and in-depth investigation of the electrocatalytic response from the MoS_2 nanosheets provides a detailed understanding of the role and the nature of defects in HER over a large range of concentrations of sulfur vacancy. Our results show that HER mechanism on defective MoS_2 is divided into two stages corresponding to: *1*) "point" defects at low concentrations of surface S-vacancies; and *2*) undercoordinated Mo regions cause by stripping of sulfur atoms at very high concentration of surface defects. The intrinsic activity of the MoS_2 – extrapolated from the turnover frequency (TOF) – suggests that the formation of undercoordinated Mo regions in MoS_2 nanosheets results in the highest catalytic activity, while amorphous molybdenum sulfide demonstrates the highest activity in an acidic medium.

RESULTS AND DISCUSSION

We synthesized MoS_2 nanosheets *via* a hydrothermal reaction in N, N-dimethylformamide (DMF) using ammonium thiomolybdate ($(NH_4)_2MoS_4$) as a precursor for both Mo and S (Figure 1a). During the synthesis, the MoS_2 nanosheets organized into nanoflower-like structures composed of few-layer stacked nanosheets (Figure 1b). At high

magnification, the layered structure of the MoS_2 is clearly visible and the length of the nanosheets is typically below 100 nm (Figures 1c,d). From the Raman spectrum of as-synthesized MoS_2 (Figure S1a), the vibration modes are weak and broad, revealing that the nanosheets are mostly amorphous in nature. The nanosheets were annealed at 800 °C under argon (MoS_2-8A) to obtain highly crystalline nanosheets of the trigonal prismatic (2H) phase – as confirmed by the strong and sharp E^1_{2G} and A_{1G} modes at 385 cm^{-1} (in-plane vibration modes) and 410 cm^{-1} (out-of-plane vibration modes), respectively (Figure S1a). We note that the pristine 2H MoS_2 keeps the same nanoflower-like structures as as-synthesized MoS_2. The high crystallinity of the pristine 2H MoS_2 nanosheets was observed under high resolution electon transmission microscopy and high annular angle dark field scanning transmission electron transmission microscopy (HAADF-STEM) (Figures S1b-d). The spacing of the nanosheets is found to be ~ 6.5 Å $\pm$ 0.04. Different strategies have been reported for defect engineering in 2D TMDs: including hydrothermal growth,[51] plasma,[52,53] electrochemical desulfurization[54] or chemical treatments.[55] In this work, sulfur vacancies were introduced in the 2H MoS_2 lattice by annealing the nanosheets under hydrogen (H_2) at increasing temperatures from 400 °C up to 800 °C (Figure 1a). H_2 annealing enables good control of the defect formation while being scalable.[44] The final samples are labeled as MoS_2-*x*H, where *x* represents the annealing temperature under hydrogen (for example, MoS_2-4H for 400 °C annealing under H_2 atmosphere). Defects in the structure of the 2H MoS_2 nanoflowers have been observed under the electron microscope and typical defects consist of cracks and misaligned basal planes as previously observed in the literature (Figure 2a,b).[50,57] After annealing under hydrogen, additional defects in the form of sulfur atom vacancies are observed on the MoS_2 basal planes. Figure 2c shows a representative high resolution TEM image of an ultra-thin layer of defected MoS_2-7H. The expected hexagonal

symmetry is clearly visible together with a high density of defects – identified as slightly brighter spots in position of sulfur atoms (Figure 2c, red cycles) as previously reported in the literature.[58,59] We also performed energy dispersive X-ray mapping of the Mo and S elements on the MoS_2 nanoflowers (Figures 2d-f). The signals from S atoms from pristine 2H MoS_2 exhibit higher density compared to the ones from Mo atoms as expected for a S:Mo ratio of ~ 2. In contrast, defected MoS_2-7H displays weaker contrast between the Mo and S maps (Figures 2g-i). This observation first hints that a significant portion of the sulfur atoms has been removed from the MoS_2 basal plane after annealing under hydrogen forming abundant sulfur vacancies.

While electron microscopy provides local information at the nanoscale level, we also probed the nature of the defects in the MoS_2 nanosheets over large regions by notably using X-ray diffraction (XRD), electron paramagnetic resonance (EPR) and X-Ray photoelectron spectroscopy [See the Supplementary Information (SI) for details about the measurements]. After annealing at 800 °C under Argon, the signatures of the 2H polymorph of MoS_2 are visible in the diffraction pattern. The (002) peak is clearly detected at 14° – strongly enhanced compared to the case of as-synthesized MoS_2 for which the (002) peak is split between 10° and 14° (Figure S2a). When increasing the annealing temperatures under hydrogen, all the MoS_2 signatures decrease suggesting a reduced crystallinity of the material (Figure S2b). The intensity of the (100) peak decreases faster than the (002) peak indicating that the formation of defects does not dramatically affect the layered structure (Figure S3a) of MoS_2. This is in perfect agreement with high-resolution Transmission Electron Microscope images showing an average interlayer spacing of 6.62 Å ± 0.01 for MoS_2-7H. We note that the full width at half maximum (FWHM) of the (100) peak gets larger as the temperature is increased, while the crystallite size reduces (Figure S3b). This is in agreement with the progressive formation of defects in the MoS_2 basal planes. It is

worth noting that the degradation of crystallinity accelerates after 600 °C. Similar trends are also observed in the Raman spectra where the E^1_{2G} and A_{1G} peaks shift towards lower and higher frequencies respectively as the annealing temperature increases (Figure S4). These displacements are accompanied by a progressive broadening of the vibrational modes as previously observed for ion-bombarded MoS_2.[60]

Next, we performed Electron Paramagnetic Resonance (EPR) at increasing temperatures for 2H MoS_2 under H_2 in order to estimate the evolution of the concentration of sulfur vacancies (See methods in SI). The signature of the Mo-S dangling bonds can be detected at ~ 3500 G and the signal is expected to be proportional to the concentration of dangling bonds from the S-vacancies in the MoS_2 slabs (Figure 3a).[55] We found that pristine 2H MoS_2 (MoS_2-8A) presents some EPR signals suggesting that as-synthesized materials possess some defects as expected for solution-processed materials. As the H_2 annealing temperature increases, we observed that the signature from the S-vacancies increases up to 600 °C, after which, the signal rapidly decreases (Inset of Figure 3a). The decrease of the signal from the S-vacancies reveals a decrease in the amount of Mo-S dangling bonds in the MoS_2 nanosheets after 600 °C. This is in apparent contradiction with the formation of S-vacancies as the temperature increases. We attribute this behavior to a change in the nature of the defects. Below 600 °C "point" defects are created and generate Mo-S dangling bonds responsible for the EPR signals. Beyond 600 °C, the S atoms start to get stripped leading to larger defects. The quantity of Mo-S dangling bonds in the MoS_2 slab is thus expected to decrease leading to weaker EPR signals. The evolution of the structure of the MoS_2 nanosheets upon annealing is summarized in Figure 1a. X-ray photoelectron spectroscopy was used to further investigate the nature of the defects in the MoS_2-*x*H samples. Figure 3b shows the Mo3d and S2s regions from the different 2H MoS_2. For pristine 2H MoS_2 (MoS_2-8A), signals are

detected at 229.7 eV and 232.8 eV corresponding to the $Mo3d_{5/2}$ and the $Mo3d_{3/2}$, respectively, and attributed to Mo(+IV) in MoS_2, whereas the signals at 226.9 eV originate from the S2s electrons. We note that no signals from oxidized Mo(+VI) – expected at 232.2 and 235.5 eV from Mo(+VI)3d5/3 and Mo(+VI)3d3/2 (Ref. 41) – can be detected, which confirms the absence of oxidation for the different MoS_2 samples. The Mo 3d and S 2s signals remain virtually constant up to 600 °C after which, the signals from Mo(+IV) and S 2s rapidly decrease. This decrease is accompanied by the emergence of a new doublet at 228.5 eV and 231.7 eV attributed to undercoordinated molybdenum: Mo(*UC*). By measuring the signals from the Mo 3d and the S 2p regions, it is possible to determine the S:Mo ratio as a function of the annealing temperature (Figure 3c). The quantitative data from the XPS analyses was further confirmed by ICP-AES analyses of as-synthesized MoS_2 and MoS_2-8H (Figure S6). The low S:Mo ratio for MoS_2-8H combined with the absence of Raman signals (Figure S1) suggest that the majority of the structure of MoS_2 is not preserved after annealing. On the other hand, the XPS analyzes of MoS_2-7H reveal a very low S:Mo ratio at about 0.5, which may appear to be in contradiction with the amount of S atoms detected from the energy dispersive X-ray mapping shown in Figure 2h,i. We attribute this to a difference of composition between surface and bulk of the MoS_2 nanoflowers. Indeed, the majority of stripped S atoms originates from the surface of the nanosheets, while the other S atoms from the inner layers of the MoS_2 nanoflowers are more stable and less prone to react with H_2. Therefore the elemental mapping images shown in Figure 2 indicate both surface and bulk compositions, whereas the XPS analyzes only reflects the surface composition. The formation of defects is visible on the HR-TEM images from the disordered section on the outer layer of the MoS_2 nanosheets while the multilayered nature of the MoS_2 is not affected (Figure S7). This is also supported by the obvious XRD and Raman

signatures from MoS_2 up to 700 °C confirming that the bulk section of the MoS_2 nanoflowers are preserved. Thus the multilayered nature of the MoS_2 nanosheets allows maintaining the structural integrity of the nanoflowers as the formation of defects mainly occurs at the surface section, *i.e.* the outer MoS_2 layer of the nanoflowers. Our results are in line with previous reports from the literature for encapsulated TMDs.[61-63] From Figure 3c, two stages are clearly observed: a first stage where the S:Mo ratio decreases from ~ 2.1 to 1.7 for T < 600 °C and a second stage for T > 600 °C where the S:Mo ratio decreases from 1.7 to 0.2 from 600 °C to 800 °C. A similar trend as for the S:Mo ratio is observed by plotting the Mo(*UC*):Mo(+IV) ratio demonstrating that the formation of the Mo(*UC*) and the extent of S-vacancies are strongly related (Inset of Figure 3c). Both EPR and XPS analysis qualitatively agree on the existence of 2 stages corresponding to different natures of defects: "point" defects below 600 °C and S-stripping with formation of undercoordinated Mo above 600 °C.

We evaluated the electrocatalytic response of the MoS_2 samples towards the evolution of hydrogen reaction (HER). In order to gain deeper insight into the role of structure and S-vacancies on the electrocatalytic performance, HER performance was investigated in both acidic and basic media in order to vary the concentration of protons (H^+) present in the solution (See HER measurements in the Methods section). We first compare the activity of amorphous and crystalline 2H MoS_2 by recording the polarization curves in different electrolytes (Figure S8). Amorphous and 2H MoS_2 exhibit the largest current density in 0.5 M H_2SO_4 (pH=0.6, denoted as pH≈0) and in 0.1 M KOH (pH=12.9, denoted as pH≈13) respectively. It is well known that the current density can be influenced by external factors such as the surface morphology of the electrode. In order to have a more accurate estimation of the intrinsic catalytic activity, we estimated the Turnover Frequency (TOF): $\frac{n_{H_2}}{n_{active\ sites}}$ of the different MoS_2 electrodes based on

the measurement of the electrochemically active surface area (ECSA) (See "TOF calculations" section in the Methods section). Figure 3d shows the TOF from amorphous and crystalline 2H MoS_2 electrodes at pH≈0 and pH≈13. The values of TOF show a clear dependence on the concentration of protons in the case of amorphous MoS_2 and the catalytic activity is clearly enhanced at high concentrations of protons in the electrolyte solution. In 0.5 M H_2SO_4, amorphous MoS_2 clearly evolves hydrogen at a minimal overpotential of ~ 100 mV and a low Tafel slope of 44 mV dec^{-1} (Figure S9), while the activity is strongly reduced in 0.1 M KOH. Conversely, the change of the activity between pH≈0 and pH≈13 is marginal in the case of 2H MoS_2 and the overpotential together with the Tafel slopes remain virtually constant. Our results reveal that the HER activity is proton mediated ($H^+ + e^- \rightarrow H^*$) in the case of amorphous MoS_2 whereas for 2H MoS_2, the HER can proceed *via* either direct proton adsorption $H^+ + e^- \rightarrow H^*$ or the dissociation of a water molecule:$H_2O + e^- \rightarrow H^* + HO^-$.

To get deeper understanding of the role of surface S-vacancies on the HER activity we systematically measured the different MoS_2-*x*H electrodes with known concentrations of defects in both electrolytes. Figures 4a,b show the polarization curves for 2H MoS_2-*x*H at pH≈0 and pH≈13. In both acidic and basic media, the electrocatalytic performance of the 2H MoS_2 electrodes gradually improves as the concentration of defects increases. This improvement originates from the reduction of the overpotential combined with the decrease of the Tafel slope (Figure S10). The value of Tafel slope of pristine 2H MoS_2 (MoS_2-8A) is estimated to be ~ 110 mV dec^{-1} in 0.5 M H_2SO_4 in good agreement with the previous results from the literature.[55,64-66] This value is slightly larger in 0.1 M KOH and the Tafel slope reaches ~ 120 mV dec^{-1}. When the quantity of S-vacancies increases – with increasing annealing temperature – the Tafel slope reduces to ~ 80 mV dec^{-1} for both electrolyte solutions. When carefully examining the evolution

of the Tafel slopes with the temperature, two different behaviors can be observed (Figure 4c). In 0.1 M KOH, the Tafel slopes linearly decrease with temperature. Conversely, in 0.5 M H_2SO_4, the Tafel slopes first decrease from 110 mV dec^{-1} down to 85 mV dec^{-1} for the MoS_2-6H and then stabilize. When plotting the Tafel slopes as function of the S:Mo ratio, two regimes corresponding to the two stages with point defects (Stage 1) and S-stripping (Stage 2) are clearly visible (Figure S11). At both pH values, the Tafel slopes decrease faster upon the creation of point defects in the 2H MoS_2 slabs demonstrating a clear improvement of the reaction kinetics. In the regime of S-stripping, the Tafel slope further improves at a slower rate in the basic medium, while much slower improvements are measured in the acidic medium.

The double-layer capacitance (C_{dl}) of 2H MoS_2 and MoS_2-*x*H electrodes has been estimated by cycling the different electrodes at increasing scan rates (See "Double-layer capacitance measurements" section in the Methods section). As the concentration of defects increases, the C_{dl} gets larger suggesting larger number of electrochemically active sites at the electrodes surface (Figure S12). When reaching the domain (Stage 2) of S-stripping, the C_{dl} saturates in the basic medium and eventually decreases in the case of the acidic medium. Combining C_{dl} and polarization curves, we then calculated the TOF for different electrodes (Figures 4d,e). Figure 4f shows the evolution of the TOF measured at η = 300 mV in acidic and basic media as a function of annealing temperature. In 0.1 M KOH, as annealing temperature is increased, the TOF continuously increases up to 800 °C. This improvement is explained by the linear decrease of the Tafel slope combined with the reduction of the overpotential. Interestingly, the evolution of the TOF is different in 0.5 M H_2SO_4, for which TOF values stabilize at temperatures higher than 600 °C, reflecting the saturation of the Tafel slopes. The exchange current density (j_0) was determined by extrapolating the Tafel plot to investigate the intrinsic

HER activity from different MoS_2-*x*H samples. Both in acidic and basic media, the exchange current density gradually increases with the increase of H_2-annealing temperature (Figure S13a,c). The ECSA-normalized exchange current densities of MoS_2-7H reach 0.19 ±0.004 and 0.35±0.04 μA cm^{-2}_{ECSA} for pH≈0 and pH≈13, respectively. We measured the charge transfer resistance (Z_{CT}) in both acidic and basic media using electrochemical impedance spectroscopy (See "Electrochemical Impedance measurements" section in the Methods section). Similar to the evolution of the TOF, Z_{CT} continuously decreases before saturating after 600 °C (Figure S14). The rapid reduction of Z_{CT} at T < 600 °C indicates that the injection of the electrons in the presence of point defect S-vacancies is facilitated independently of the concentration of protons in the electrolyte. In order to demonstrate the role of the surface S-vacancies on the improvement of the HER activity, we repaired the defected MoS_2 electrodes by annealing the S-vacancies under sulfur atmosphere (See "Healing defected MoS_2 electrodes" section in the Methods section). We note that while the 2H MoS_2 structure is confirmed using XPS and Raman spectroscopy (Figures 3 and S4), the Raman signatures from repaired 2H-MoS_2 display larger FWHM (full width at half maximum) suggesting that the MoS_2 structure is not fully restored. The repaired 2H-MoS_2 electrode (MoS_2-7S) performs similarly in both acidic and basic media compared to pristine 2H MoS_2 (MoS_2-8A) as shown from the polarization curves (Figure S15). This result is further confirmed by calculating the values of TOF frequency (Figure S16). More importantly, the repaired 2H-MoS_2 electrodes exhibit nearly successful restoration towards some key electrocatalytic parameters in both acidic and basic media, such as *i)* the Tafel slope (Figure 4c and Figure S11), *ii)* the TOF measured at η = 300 mV (Figure 4f and Figure 5b,c), *iii)* the overpotential at 10 mA cm^{-2} (Figure 4f and Figure 5b,c) and *iv)* the overpotential at TOF=2 s^{-1} (Figure 5a). We also applied the same methodology on chemically exfoliated single-layer MoS_2

nanosheets and the same trends as for MoS_2 nanosheets grown *via* hydrothermal reaction were observed (Figure S17-18). Overall our measurements clearly supports that the enhancement of the performance is primarily due to the surface S-vacancies.

Stability is an important parameter in electrocatalysis as the electrodes must be able to sustain fixed current over a large period of time. We measured the stability of the 2H MoS_2 with and without S-vacancies at a fixed current density of 10 mA cm^{-2} – corresponding to approximately 10 % efficiency in a solar-driven water splitting system. Figure S21 shows evolution of the overpotential at 10 mA cm^{-2} over 24 hours for MoS_2-5H and MoS_2-7H corresponding to point defect and S-stripping regimes respectively. Both samples are found to be stable in acidic and basic media with a minimal increase of the overpotential of less than 90 mV. The chronopotentiometry measurements thus demonstrate that the active sites formed by the S-vacancies are stable and validate the defect engineering strategy for increasing the intrinsic electrocatalytic activity of 2H MoS_2.

To further understand the role and the nature of the surface S-vacancies on the electrocatalytic response of the 2H MoS_2 electrodes, we then analyzed the HER performance relative to the S:Mo ratio. Figure 5a shows the required overpotentials for reaching a TOF of 2 s^{-1} in acidic and basic media. The overpotential at 2 s^{-1} decreases rapidly when decreasing the S:Mo ratio from ~ 2 to ~ 1.7 corresponding to the limit of the point defect regime (Stage 1). Below S:Mo ~ 1.7 (Stage 2), the overpotential decreases further – albeit at a slower rate. We also analyzed the evolution of the overpotential (η) and of the TOF at a fixed overpotential of 300 mV with the S:Mo ratio in 0.5 M H_2SO_4 and 0.1 M KOH (Figure 5b,c). Expectedly, both parameters: η and the TOF are found to be strongly correlated to the S:Mo ratio. A similar dependency is obtained when plotting the overpotential and the TOF at 300 mV overpotential as

a function of the Mo-S dangling bond signals detected in EPR spectroscopy (Figure S22). Such strong dependence highlights the role of the MoS_2 structure on the performance and calls for additional investigations of the HER mechanism notably using numerical simulations. At defect concentrations < 15%, the HER performance of 2H MoS_2 increases rapidly as evidenced by the increase of the TOF values and the decrease of the overpotentials. This is attributed to the decrease of the Tafel slopes and the overpotentials in agreement with previous results from the literature.[53] Very interestingly, our results demonstrate that undercoordinated Mo atoms formed by stripping the surface-sulfur atoms from the basal planes can further increase the HER performance. The enhancement of the HER activity is observed in both acidic and basic media although the largest improvements are observed in 0.1 M KOH, for which the overpotential decreases from 420 mV to 260 mV while the TOF increases from < 1 s^{-1} to 15 s^{-1}. Finally Figure 6 presents the TOF values from amorphous and MoS_2-7H together with those obtained from other low dimensional electrocatalysts reported in the literatures.[67-77] One can see that MoS_2-7H compares favorably with most electrocatalysts and larger TOF are observed at pH≈13, unambiguously demonstrating the promise of defect engineering for the controlled formation of undercoordinated Mo region within the MoS_2 slabs. We also note that the preparation of defect-engineered MoS_2 *via* H_2 annealing has the advantages of being more controllable and scalable compared to other nanostructures.

CONCLUSION

The above experiments provide an in-depth insight into the role of the structure and surface sulfur vacancies on the HER performance of MoS_2. The role of surface sulfur vacancies from multilayered MoS_2 was explored over large range surface concentrations from 0 up to 90%.

Amorphous MoS_2 and defective 2H MoS_2 demonstrated the highest HER performance in acidic and basic electrolytes, respectively, suggesting different reaction pathways. Combining various physical characterization techniques, we identified two stages corresponding to point defects for S:Mo > 1.7 and undercoordinated Mo atoms for large defects formed during sulfur stripping from the basal plane at S:Mo < 1.7. We observed that the existence of the two different domains of surface S-vacancies translate into two different regimes in HER. Point-defects lead to a rapid increase of the HER activity as confirmed by the TOF and overpotential values. We identified that large densities of vacancies *via* S-stripping further improve the HER performance– albeit at a slower rate – through the formation of domains of undercoordinated Mo. Based on our results, we propose that combination of local point defects with undercoordinated Mo regions could be a strategy for maximizing the density of active sites on the MoS_2 nanosheets. These findings shed light on the importance of the structure and nature of defects for improving the electrocatalytic activity of 2H MoS_2 towards HER for the production of hydrogen in both acidic and basic media.

METHODS

MoS_2 synthesis

20 mg of $(NH_4)_2MoS_4$ was dispersed in 35 ml of DMF followed by sonication at room temperature for 10 min until a homogeneous, red-brown solution was achieved. The mixture solution was transferred into a 50 mL Teflon-lined autoclave and maintained at 210 °C for 36 h in an electrical oven. The product was collected by centrifugation at 12000 rpm for 30 min, washed with ethanol and recollected by centrifugation. The washing step was repeated for at

least 4 times to remove residual DMF. Finally, the product was dispersed in 12.3 mL of ethanol to make the black ink (1 mg/ml) for electrochemical measurements.

Preparation of 2H MoS_2 and MoS_2-*x*H electrodes

The working electrode was prepared by drop casting 10 μL of ink onto a pure glassy carbon electrode (diameter = 4 mm). The electrode (hereafter termed "MoS_2-AS") was dried at room temperature before electrochemical measurements. As-prepared working electrodes were then annealed in a tube furnace under ultra-purity argon at 800 °C (ramping rate of 5 °C/min) for 1 h. The quartz tube containing the MoS_2-AS electrodes was purged with argon for 30 min to remove any trace of oxygen. The temperature of the furnace was quickly elevated to 800 °C (ramping rate of 10 °C/min) and kept at 800 °C for 1 hour. The obtained working electrodes are denoted MoS_2-8A. Sulfur vacancies were generated in the MoS_2 slabs by further annealing under hydrogen (5% in argon, Varygon®) under vacuum at temperatures varying from 400 °C to 800 °C for 30 min with a 10 °C min^{-1} ramping rate. The obtained electrodes were denoted as MoS_2-4H, MoS_2-5H, MoS_2-6H, MoS_2-7H, MoS_2-8H for 400 °C, 500 °C, 600 °C, 700 °C and 800 °C respectively.

Healing defected MoS_2

Repaired MoS_2 electrodes were prepared by annealing MoS_2-8H under Argon in a sulfur-rich atmosphere. MoS_2-8H electrodes were placed at the center of a tube furnace and 0.5 g of sulfur were placed at the entrance of the furnace. After purging the tube with argon for 30 min, the temperature of the furnace was quickly elevated to 750 °C (ramping rate of 10 °C/min), kept at 750 °C for 30 min and finally cooled down to room temperature. The healed defected MoS_2 is denoted as MoS_2-7S.

Electrochemical measurements

Electrochemical HER measurements were performed on an potentiostat (VSP from Biologic Science Instruments) with a three-electrode cell configuration. Glassy carbon electrodes were used as working electrodes, whereas a saturated calomel electrode (SCE) and a graphite rod were used as reference and counter electrodes, respectively. All potentials were referenced to the reversible hydrogen electrode (RHE) by the equation $E_{RHE} = E_{SCE} + 0.241 + 0.0591 \times pH$. The HER performance was measured in an N_2-saturated 0.5 M H_2SO_4 (pH ≈ 0) and 0.1 M KOH (pH ≈ 13) electrolyte at a scan rate of 5 mV s^{-1}. Prior to any measurements, the electrodes were cycled 20 times in order to stabilize the electrochemical responses. The electrochemical stability tests were conducted by chronopotentiometry at 10 mA cm^{-2} for 24 h. To evaluate the electrochemical active surface area (ECSA), CV was conducted from 0.12 V to 0.22 V (in 0.5 M H_2SO_4) and 0.1 V to 0.2 V (in 0.1 M KOH) *vs* RHE with different sweep rates between 10 and 80 mV s^{-1}. Measurements of the double-layer capacitance were carried out by cycling the electrodes between 0.12 to 0.22 V (in 0.5 M H_2SO_4) and 0.1 to 0.2 V (in 0.1 M KOH) *vs.* RHE at increasing sweep rates between 10 and 80 mV s^{-1}.

TOF calculations

The turnover frequency (TOF) is defined as the number of turnovers per active site per second. The TOF was calculated from the current density normalized to the surface of MoS_2 exposed using the following relation:

$$\mathrm{TOF} = \frac{J \times N_A}{2n \times F \times ECSA}$$

,where J is the current density, N_A is Avogadro's number (6.023×10^{23}), 2 represents the stoichiometric number of electrons exchanged during the HER reaction, n is the number of active sites per cm^2 for a flat surface of MoS_2, F is the Faraday constant (96485 C mol^{-1}), and ECSA is

the electrochemically active surface area of the electrode. The number of active sites was estimated by assuming all surface S atoms are active. The error bars in Figure 6b correspond to hydrogen coverage of ¼ (Ref. 78) and $^1/_{16}$ (Ref. 44) based on previous numerical calculations of the free energy of hydrogen storage ($\Delta G°_{H*}$) The electrochemically active surface area (ECSA) was calculated from the ratio of the measured double-layer capacitance with respect to the specific capacitance of an atomically smooth MoS_2 material (60 μF cm^{-2}).[65]

Calculation of the exchange current density

The exchange current density (j_0) is calculated by fitting the linear portion of the Tafel plot to the Tafel equation ($\eta = b \log |j| + a$, where η is overpotential, j is the current density, b is the Tafel slope, and a is the intercept of the Tafel plot).

ASSOCIATED CONTENT

Supporting Information

Physical characterizations; Raman spectroscopy and electron microscopy; X-Ray diffraction; ICP-AES analyses; HR-TEM observation of the outer layer of MoS_2-8A and MoS_2-7H; Influence of the crystallinity of MoS_2 on the HER performance; Evolution of the Tafel slopes for the MoS_2-*x*H samples; Double-layer capacitance (C_{dl}) measurements for the MoS_2-*x*H samples; Exchange current density for the MoS_2-*x*H samples; Electrochemical Impedance measurements for the MoS_2-*x*H samples; HER performance from repaired MoS_2; HER performance from chemically exfoliated 1T MoS_2 nanosheets and their derivatives; Influence of the annealing steps; Stability measurements; TOF *vs*. EPR signals; Comparison of TOF in alkaline and acid media of MoS_2 with literature data. The Supporting Information is available free of charge *via* the Internet at http://pubs.acs.org.

AUTHOR INFORMATION

Corresponding Author

* Email: damien.voiry@umontpellier.fr

ORCID

Damien Voiry: 0000-0002-1664-2839

Competing financial interests

The authors declare no competing financial interests.

ACKNOWLEDGMENTS

D.V. acknowledges financial support from the US Army RDECom Grant N°W911NF-17-2-0033, the CNRS Cellule Energie exploratory Project: "R2D-CO2". This project has also received partial funding from the European Research Council (ERC) under the European Union's Horizon 2020 research and innovation programme (grant agreement No 804320). L.L. acknowledges National Natural Science Foundation of China (21503092) and Zhejiang Provincial Natural Science Foundation of China (LY19B030005). L.R. acknowledges scholarship from the Graduate School "Ecole doctorale des Sciences Chimiques, ED 459". We thank Corine Reibel and Dr. Erwan Oliviero for the electron paramagnetic resonance and electron microscopy respectively.

REFERENCES

(1) Liu, M.; Zhang, R.; Chen, W. Graphene-Supported Nanoelectrocatalysts for Fuel Cells: Synthesis, Properties, and Applications. *Chem. Rev.* **2014**, *114*, 5117-5160.

(2) Peng, S.; Han, X.; Li, L.; Chou, S.; Ji, D.; Huang, H.; Du, Y.; Liu, J.; Ramakrishna, S. Electronic and Defective Engineering of Electrospun $CaMnO_3$ Nanotubes for Enhanced Oxygen Electrocatalysis in Rechargeable Zinc–Air Batteries. *Adv. Energy Mater.* **2018**, *8*, 1800612.

(3) Stevens, M. B.; Enman, L. J.; Batchellor, A. S.; Cosby, M. R.; Vise, A. E.; Trang, C. D. M.; Boettcher, S. W. Measurement Techniques for the Study of Thin Film Heterogeneous Water Oxidation Electrocatalysts. *Chem. Mater.* **2017**, *29*, 120-140.

(4) Li, W.; Jiang, N.; Hu, B.; Liu, X.; Song, F.; Han, G.; Jordan, T. J.; Hanson, T. B.; Liu, T. L.; Sun, Y. Electrolyzer Design for Flexible Decoupled Water Splitting and Organic Upgrading with Electron Reservoirs. *Chem* **2018**, *4*, 637-649.

(5) Liu, J.; Zheng, Y.; Zhu, D.; Vasileff, A.; Ling, T.; Qiao, S.-Z. Identification of pH-Dependent Synergy on Ru/MoS_2 Interface: A Comparison of Alkaline and Acidic Hydrogen Evolution. *Nanoscale* **2017**, *9*, 16616–16621.

(6) Chen, Y. Y.; Zhang, Y.; Zhang, X.; Tang, T.; Luo, H.; Niu, S.; Dai, Z. H.; Wan, L. J.; Hu, J. S. Self-Templated Fabrication of $MoNi_4/MoO_{3-x}$ Nanorod Arrays with Dual Active Components for Highly Efficient Hydrogen Evolution. *Adv. Mater.* **2017**, *29*, 1703311.

(7) Lassalle-Kaiser, B.; Merki, D.; Vrubel, H.; Gul, S.; Yachandra, V. K.; Hu, X.; Yano, J. Evidence from *in Situ* X-ray Absorption Spectroscopy for the Involvement of Terminal Disulfide in the Reduction of Protons by an Amorphous Molybdenum Sulfide Electrocatalyst. *J. Am. Chem. Soc.* **2015**, *137*, 314–321.

(8) Yan, M., Pan, X., Wang, P., Chen, F., He, L., Jiang, G., Wang, J., Liu, J. Z., Xu, X., Liao, X., Yang, J., Mai, L. Field-Effect Tuned Adsorption Dynamics of VSe_2 Nanosheets for Enhanced Hydrogen Evolution Reaction. *Nano Lett.* **2017**, *17*, 4109-4115.

(9) Hu, C.; Dai, L. Multifunctional Carbon-Based Metal-Free Electrocatalysts for Simultaneous Oxygen Reduction, Oxygen Evolution, and Hydrogen Evolution. *Adv. Mater.* **2017**, *29*, 1604942.

(10) Di, J.; Yan, C.; Handoko, A. D.; Seh, Z. W.; Li, H.; Liu, Z. Ultrathin Two-Dimensional Materials for Photo- and Electrocatalytic Hydrogen Evolution. *Mater. Today* **2018**, *21*, 749–770.

(11) Peng, S., Gong, F., Li, L., Yu, D., Ji, D., Zhang, T., Hu, Z., Zhang, Z., Chou, S., Du, Y., Ramakrishna, S. Necklace-like Multishelled Hollow Spinel Oxides with Oxygen Vacancies for Efficient Water Electrolysis. *J. Am. Chem. Soc*. **2018**, *140*, 13644-13653.

(12) Zhao, S., Wang, Y., Dong, J., He, C.-T., Yin, H., An, P., Zhao, K., Zhang, X., Gao, C., Zhang, L., Lv, J., Wang, J., Zhang, J., Khattak, A. M., Khan, N. A., Wei, Z., Zhang, J., Liu, S., Zhao, H., Tang, Z. Ultrathin Metal–Organic Framework Nanosheets for Electrocatalytic Oxygen Evolution. *Nat. Energy* **2016**, *1*, 16184.

(13) Voiry, D.; Shin, H. S.; Loh, K. P.; Chhowalla, M. Low-Dimensional Catalysts for Hydrogen Evolution and CO_2 Reduction. *Nat. Rev. Chem.* **2018**, *2*, 0105.

(14) Gao, S.; Lin, Y.; Jiao, X.; Sun, Y.; Luo, Q.; Zhang, W.; Li, D.; Yang, J.; Xie, Y. Partially Oxidized Atomic Cobalt Layers for Carbon Dioxide Electroreduction to Liquid Fuel. *Nature* **2016**, *529*, 68–71.

(15) Asadi, M., Kim, K., Liu, C., Addepalli, A. V., Abbasi, P., Yasaei, P., Phillips, P., Behranginia, A., Cerrato, J. M., Haasch, R., Zapol, P., Kumar, B., Klie, R. F., Abiade, J., Curtiss, L. A., Salehi-Khojin, A. Nanostructured transition Metal Dichalcogenide Electrocatalysts for CO_2 Reduction in Ionic Liquid. *Science* **2016**, *353*, 467-470.

(16) Abbasi, P.; Asadi, M.; Liu, C.; Sharifi-Asl, S.; Sayahpour, B.; Behranginia, A.; Zapol, P.; Shahbazian-Yassar, R.; Curtiss, L. A.; Salehi-Khojin, A. Tailoring the Edge Structure of Molybdenum Disulfide toward Electrocatalytic Reduction of Carbon Dioxide. *ACS Nano* **2017**, *11*, 453–460.

(17) Jia, J.; Xiong, T.; Zhao, L.; Wang, F.; Liu, H.; Hu, R.; Zhou, J.; Zhou, W.; Chen, S. Ultrathin N-Doped Mo_2C Nanosheets with Exposed Active Sites as Efficient Electrocatalyst for Hydrogen Evolution Reactions. *ACS Nano* **2017**, *11*, 12509–12518.

(18) Xu, Y.-T.; Xiao, X.; Ye, Z.-M.; Zhao, S.; Shen, R.; He, C.-T.; Zhang, J.-P.; Li, Y.; Chen, X.-M. Cage-Confinement Pyrolysis Route to Ultrasmall Tungsten Carbide Nanoparticles for Efficient Electrocatalytic Hydrogen Evolution. *J. Am. Chem. Soc.* **2017**, *139*, 5285–5288.

(19) Miao, M.; Pan, J.; He, T.; Yan, Y.; Xia, B. Y.; Wang, X. Molybdenum Carbide-Based Electrocatalysts for Hydrogen Evolution Reaction. *Chem. - Eur. J.* **2017**, *23*, 10947–10961.

(20) Abghoui, Y.; Skúlason, E. Hydrogen Evolution Reaction Catalyzed by Transition-Metal Nitrides. *J. Phys. Chem. C* **2017**, *121*, 24036–24045.

(21) Wang, Y.; Chen, L.; Yu, X.; Wang, Y.; Zheng, G. Superb Alkaline Hydrogen Evolution and Simultaneous Electricity Generation by Pt-Decorated Ni_3N Nanosheets. *Adv. Energy Mater.* **2017**, *7*, 1601390.

(22) Liao, L.; Wang, S.; Xiao, J.; Bian, X.; Zhang, Y.; Scanlon, M. D.; Hu, X.; Tang, Y.; Liu, B.; Girault, H. H. A Nanoporous Molybdenum Carbide Nanowire as an Electrocatalyst for Hydrogen Evolution Reaction. *Energy Environ. Sci.* **2014**, *7*, 387–392.

(23) Shi, Y.; Zhang, B. Recent Advances in Transition Metal Phosphide Nanomaterials: Synthesis and Applications in Hydrogen Evolution Reaction. *Chem. Soc. Rev.* **2016**, *45*, 1529–1541.

(24) Zeng, Y.; Wang, Y.; Huang, G.; Chen, C.; Huang, L.; Chen, R.; Wang, S. Porous CoP Nanosheets Converted from Layered Double Hydroxides with Superior Electrochemical Activity for Hydrogen Evolution Reactions at Wide pH Ranges. *Chem. Comm.* **2018**, *54*, 1465-1468.

(25) Shi, J., Ma, D., Han, G.-F., Zhang, Y., Ji, Q., Gao, T., Sun, J., Song, X., Li, C., Zhang, Y., Lang, X.-Y., Zhang, Y., Liu, Z. Controllable Growth and Transfer of Monolayer MoS_2 on Au Foils and Its Potential Application in Hydrogen Evolution Reaction. *ACS Nano* **2014**, *8*, 10196−10204.

(26) Liu, Z.; Gao, Z.; Liu, Y.; Xia, M.; Wang, R.; Li, N. Heterogeneous Nanostructure Based on 1T-Phase MoS_2 for Enhanced Electrocatalytic Hydrogen Evolution. *ACS Appl. Mater. Interfaces* **2017**, *9*, 25291−25297.

(27) Eng, A. Y. S.; Ambrosi, A.; Sofer, Z.; Šimek, P.; Pumera, M. Electrochemistry of Transition Metal Dichalcogenides: Strong Dependence on the Metal-to-Chalcogen Composition and Exfoliation Method. *ACS Nano* **2014**, *8*, 12185−12198.

(28) Zhao, X.; Ma, X.; Sun, J.; Li, D.; Yang, X. Enhanced Catalytic Activities of Surfactant-Assisted Exfoliated WS_2 Nanodots for Hydrogen Evolution. *ACS Nano* **2016**, *10*, 2159−2166.

(29) Xu, K.; Wang, F.; Wang, Z.; Zhan, X.; Wang, Q.; Cheng, Z.; Safdar, M.; He, J. Component-Controllable $WS_{2(1-x)}Se_{2x}$ Nanotubes for Efficient Hydrogen Evolution Reaction. *ACS Nano* **2014**, *8*, 8468−8476.

(30) Ding, Q.; Song, B.; Xu, P.; Jin, S. Efficient Electrocatalytic and Photoelectrochemical Hydrogen Generation Using MoS_2 and Related Compounds. *Chem* **2016**, *1*, 699−726.

(31) Wang, D.-Y., Gong, M., Chou, H.-L., Pan, C.-J., Chen, H.-A., Wu, Y., Lin, M.-C., Guan, M., Yang, J., Chen, C.-W., Wang, Y.-L., Hwang, B.-J., Chen, C.-C., Dai, H. Highly Active and Stable Hybrid Catalyst of Cobalt-Doped FeS_2 Nanosheets–Carbon Nanotubes for Hydrogen Evolution Reaction. *J. Am. Chem. Soc.* **2015***, 137*, 1587−1592.

(32) Tan, C., Luo, Z., Chaturvedi, A., Cai, Y., Du, Y., Gong, Y., Huang, Y., Lai, Z., Zhang, X., Zheng, L., Qi, X., Goh, M. H., Wang, J., Han, S., Wu, X.-J., Gu, L., Kloc, C., Zhang, H. Preparation of High-Percentage 1T-Phase Transition Metal Dichalcogenide Nanodots for Electrochemical Hydrogen Evolution. *Adv. Mater.* **2018**, *30*, 1705509.

(33) Hinnemann, B.; Moses, P. G.; Bonde, J.; Jørgensen, K. P.; Nielsen, J. H.; Horch, S.; Ib Chorkendorff, A.; Nørskov, J. K. Biomimetic Hydrogen Evolution: MoS_2 Nanoparticles as Catalyst for Hydrogen Evolution. *J. Am. Chem. Soc.* **2005**, *127*, 5308−5309.

(34) Li, R.; Yang, L.; Xiong, T.; Wu, Y.; Cao, L.; Yuan, D.; Zhou, W. Nitrogen Doped MoS_2 Nanosheets Synthesized *via* a Low-Temperature Process as Electrocatalysts with Enhanced Activity for Hydrogen Evolution Reaction. *J. Power Sources* **2017**, *356*, 133−139.

(35) Yin, P., Yao, T., Wu, Y., Zheng, L., Lin, Y., Liu, W., Ju, H., Zhu, J., Hong, X., Deng, Z., Zhou, G., Wei, S., Li, Y. Single Cobalt Atoms with Precise N-Coordination as Superior Oxygen Reduction Reaction Catalysts. *Angew. Chem. Int. Ed*. **2016**, *55*, 10800–10805.

(36) Qu, Y., Li, Z., Chen, W., Lin, Y., Yuan, T., Yang, Z., Zhao, C., Wang, J., Zhao, C., Wang, X., Zhou, F., Zhuang, Z., Wu, Y., Li, Y. Direct Transformation of Bulk Copper into Copper Single Sites *via* Emitting and Trapping of Atoms. *Nature Catalysis* **2018**, *1*, 781–786.

(37) Yang, L.; Jiang, S.; Zhao, Y.; Zhu, L.; Chen, S.; Wang, X.; Wu, Q.; Ma, J.; Ma, Y.; Hu, Z. Boron-Doped Carbon Nanotubes as Metal-Free Electrocatalysts for the Oxygen Reduction Reaction. *Angew. Chem. Int. Ed*. **2011**, *50*, 7132–7135.

(38) Jiao, Y.; Zheng, Y.; Davey, K.; Qiao, S. Z. Activity Origin and Catalyst Design Principles for Electrocatalytic Hydrogen Evolution on Heteroatom-Doped Graphene. *Nat. Energy* **2016**, *1*, 16130.

(39) Zou, X.; Liu, M.; Wu, J.; Ajayan, P. M.; Li, J.; Liu, B.; Yakobson, B. I. How Nitrogen-Doped Graphene Quantum Dots Catalyze Electroreduction of CO_2 to Hydrocarbons and Oxygenates. *ACS Catal.* **2017**, *7*, 6245–6250.

(40) Voiry, D.; Salehi, M.; Silva, R.; Fujita, T.; Chen, M.; Asefa, T.; Shenoy, V. B.; Eda, G.; Chhowalla, M. Conducting MoS_2 Nanosheets as Catalysts for Hydrogen Evolution Reaction. *Nano Lett.* **2013**, *13*, 6222–6227.

(41) Voiry, D.; Mohite, A.; Chhowalla, M. Phase Engineering of Transition Metal Dichalcogenides. *Chem. Soc. Rev.* **2015**, *44*, 2702–2712.

(42) Najmaei, S.; Yuan, J.; Zhang, J.; Ajayan, P.; Lou, J. Synthesis and Defect Investigation of Two-Dimensional Molybdenum Disulfide Atomic Layers. *Acc. Chem. Res.* **2015**, *48*, 31–40.

(43) Hong, J., Hu, Z., Probert, M., Li, K., Lv, D., Yang, X., Gu, L., Mao, N., Feng, Q., Xie, L., Zhang, J., Wu, D., Zhang, Z., Jin, C., Ji, W., Zhang, X., Yuan, J., Zhang, Z. Exploring Atomic Defects in Molybdenum Disulphide Monolayers. *Nat. Comm.* **2015**, *6*, 6293.

(44) Voiry, D., Yamaguchi, H., Li, J., Silva, R., Alves, D. C., Fujita, T., Chen, M., Asefa, T., Shenoy, V. B., Eda, G., Chhowalla, M. Enhanced Catalytic Activity in Strained Chemically Exfoliated WS_2 Nanosheets for Hydrogen Evolution. *Nat. Mater.* **2013**, *12*, 850–855.

(45) Ye, G.; Gong, Y.; Lin, J.; Li, B.; He, Y.; Pantelides, S. T.; Zhou, W.; Vajtai, R.; Ajayan, P. M. Defects Engineered Monolayer MoS_2 for Improved Hydrogen Evolution Reaction. *Nano Lett.* **2016**, *16*, 1097–1103.

(46) Li, G., Zhang, D., Qiao, Q., Yu, Y., Peterson, D., Zafar, A., Kumar, R., Curtarolo, S., Hunte, F., Shannon, S., Zhu, Y., Yang, W., Cao, L. All The Catalytic Active Sites of MoS_2 for Hydrogen Evolution. *J. Am. Chem. Soc.* **2016**, *138*, 16632–16638.

(47) Yin, Y., Zhang, Y., Gao, T., Yao, T., Zhang, X., Han, J., Wang, X., Zhang, Z., Xu, P., Zhang, P., Cao, X., Song, B., Jin, S. Synergistic Phase and Disorder Engineering in 1T-$MoSe_2$ Nanosheets for Enhanced Hydrogen-Evolution Reaction. *Adv. Mater.* **2017**, *29*, 1700311.

(48) Park, S.; Park, J.; Abroshan, H.; Zhang, L.; Kim, J. K.; Zhang, J.; Guo, J.; Siahrostami, S.; Zheng, X. Enhancing Catalytic Activity of MoS_2 Basal Plane S-Vacancy by Co Cluster Addition. *ACS Energy Lett*. **2018**, *3*, 2685–2693.

(49) Voiry, D., Fullon, R., Yang, J., de Carvalho Castro, E. S. C., Kappera, R., Bozkurt, I., Kaplan, D., Lagos, M. J., Batson, P. E., Gupta, G., Mohite, A. D., Dong, L., Er, D., Shenoy, V. B., Asefa, T., Chhowalla, M. The Role of Electronic Coupling Between Substrate and 2D MoS_2 Nanosheets in Electrocatalytic Production of Hydrogen. *Nat. Mater.* **2016**, *15*, 1003–1009.

(50) Xie, J.; Zhang, H.; Li, S.; Wang, R.; Sun, X.; Zhou, M.; Zhou, J.; Lou, X. W.; Xie, Y. Defect-Rich MoS_2 Ultrathin Nanosheets with Additional Active Edge Sites for Enhanced Electrocatalytic Hydrogen Evolution. *Adv. Mater.* **2013**, *25*, 5807–5813.

(51) Xu, Y.; Wang, L.; Liu, X.; Zhang, S.; Liu, C.; Yan, D.; Zeng, Y.; Pei, Y.; Liu, Y.; Luo, S. Monolayer MoS_2 with S Vacancy from Interlayer Spacing Expanded Counterparts for Highly Efficient Electrochemical Hydrogen Production. *J. Mater. Chem. A* **2016**, *4*, 16524–16530.

(52) Cheng, C.-C.; Lu, A.-Y.; Tseng, C.-C.; Yang, X.; Hedhili, M. N.; Chen, M.-C.; Wei, K.-H.; Li, L.-J. Activating Basal-Plane Catalytic Activity of Two-Dimensional MoS_2 Monolayer with Remote Hydrogen Plasma. *Nano Energy* **2016**, *30*, 846–852.

(53) Li, H., Tsai, C., Koh, A. L., Cai, L., Contryman, A. W., Fragapane, A. H., Zhao, J., Han, H. S., Manoharan, H. C., Abild-Pedersen, F., Norskov, J. K., Zheng, X. Activating and Optimizing MoS_2 Basal Planes for Hydrogen Evolution Through the Formation of Strained Sulphur Vacancies. *Nat. Mater.* **2016**, *15*, 364.

(54) Tsai, C.; Li, H.; Park, S.; Park, J.; Han, H. S.; Norskov, J. K.; Zheng, X.; Abild-Pedersen, F. Electrochemical Generation of Sulfur Vacancies in the Basal Plane of MoS_2 for Hydrogen Evolution. *Nat. Comm.* **2017**, *8*, 15113.

(55) Yin, Y., Han, J., Zhang, Y., Zhang, X., Xu, P., Yuan, Q., Samad, L., Wang, X., Wang, Y., Zhang, Z., Zhang, P., Cao, X., Song, B., Jin, S. Contributions of Phase, Sulfur Vacancies, and

Edges to the Hydrogen Evolution Reaction Catalytic Activity of Porous Molybdenum Disulfide Nanosheets. *J. Am. Chem. Soc.* **2016**, *138*, 7965–7972.

(56) Wiensch, J. D.; John, J.; Velazquez, J. M.; Torelli, D. A.; Pieterick, A. P.; McDowell, M. T.; Sun, K.; Zhao, X.; Brunschwing, B. S.; Lewis, N. S. Comparative Study in Acidic and Alkaline Media of the Effects of pH and Crystallinity on the Hydrogen-Evolution Reaction on MoS_2 and $MoSe_2$. *ACS Energy Lett*. **2017**, *2*, 2234–2238.

(57) Zhao, Z., Qin, F., Kasiraju, S., Xie, L., Alam, M. K., Chen, S., Wang, D., Ren, Z., Wang, Z., Grabow, L. C., Bao, J. Vertically Aligned MoS_2/Mo_2C hybrid Nanosheets Grown on Carbon Paper for Efficient Electrocatalytic Hydrogen Evolution. *ACS Catal.* **2017**, *7*, 7312-7318.

(58) Qiu, H., Xu, T., Wang, Z., Ren, W., Nan, H., Ni, Z., Chen, Q., Yuan, S., Miao, F., Song, F., Long, G., Shi, Y., Sun, L., Wang, J., Wang, X. Hopping Transport Through Defect-Induced Localized States in Molybdenum Disulphide. *Nat. Comm.* **2013**, *4*, 2642.

(59) Yu, Z., Pan, Y., Shen, Y., Wang, Z., Ong, Z., Xu, T., Xin, R., Pan, L., Wang, B., Sun, L., Wang, J., Zhang, G., Zhang, Y. W., Shi, Y., Wang, X. Towards Intrinsic Charge Transport in Monolayer Molybdenum Disulfide by Defect and Interface Engineering. *Nat. Comm.* **2014**, *5*, 5290.

(60) Lin, Z.; Carvalho, B. R.; Kahn, E.; Lv, R.; Rao, R.; Terrones, H.; Pimenta, M. A.; Terrones, M. Defect Engineering of Two-Dimensional Transition Metal Dichalcogenides. *2D Mater.* **2016**, *3*, 022002.

(61) Zan, R.; Ramasse, Q. M.; Jalil, R.; Georgiou, T.; Bangert, U.; Novoselov, K. S. Control of Radiation Damage in MoS_2 by Graphene Encapsulation. *ACS Nano* **2013**, *7*, 10167–10174.

(62) Algara-Siller, G.; Kurasch, S.; Sedighi, M.; Lehtinen, O.; Kaiser, U. The Pristine Atomic Structure of MoS_2 Monolayer Protected from Electron Radiation Damage by Grapheme. *Appl. Phys. Lett*. **2013**, *103*, 203107.

(63) Ahn, S.; Kim, G.; Nayak, P. K.; Yoon, S. I.; Lim, H.; Shin, H. J.; Shin, H. S. Prevention of Transition Metal Dichalcogenide Photodegradation by Encapsulation with h-BN Layers. *ACS Nano* **2016**, *10*, 8973–8979.

(64) Chang, K.; Hai, X.; Pang, H.; Zhang, H.; Shi, L.; Liu, G.; Liu, H.; Zhao, G.; Li, M.; Ye, J. Targeted Synthesis of 2H- and 1T-Phase MoS_2 Monolayers for Catalytic Hydrogen Evolution. *Adv. Mater.* **2016**, *28*, 10033–10041.

(65) Guo, B.; Yu, K.; Li, H.; Song, H.; Zhang, Y.; Lei, X.; Fu, H.; Tan, Y.; Zhu, Z. Hollow Structured Micro/Nano MoS_2 Spheres for High Electrocatalytic Activity Hydrogen Evolution Reaction. *ACS Appl. Mater. Interfaces* **2016**, *8*, 5517−5525.

(66) Zhang, J.; Wu, J.; Guo, H.; Chen, W.; Yuan, J.; Martinez, U.; Gupta, G.; Mohite, A.; Ajayan, P. M.; Lou, J. Unveiling Active Sites for the Hydrogen Evolution Reaction on Monolayer MoS_2. *Adv. Mater.* **2017**, *29*, 1701955.

(67) Hu, J.; Huang, B.; Zhang, C.; Wang, Z.; An Y.; Zhou, D.; Lin, H.; Leung, M. K. H.; Yang, S. Engineering Stepped Edge Surface Structures of MoS_2 Sheet Stacks to Accelerate the Hydrogen Evolution Reaction. *Energy Environ. Sci.* **2017**, *10*, 593−603.

(68) Zhou, H., Yu, F., Huang, Y., Sun, J., Zhu Z., Nielsen, R. J., He, R., Bao, J., Goddard III, W. A., Chen, S., Ren, Z. Efficient Hydrogen Evolution by Ternary Molybdenum Sulfoselenide Particles on Self-standing Porous Nickel Diselenide Foam. *Nat. Comm*. **2016**, *7*, 12765.

(69) Yan, H.; Tian, C.; Wang, L.; Wu, A.; Meng, M.; Zhao, L.; Fu, H. Phosphorus-Modified Tungsten Nitride/Reduced Graphene Oxide as a High-Performance, Non-Noble-Metal Electrocatalyst for the Hydrogen Evolution Reaction. *Angew. Chem. Int. Ed*. **2015**, *54*, 6325−6329.

(70) Ye, R., del Angel-Vicente, P., Liu, Y., Josefina Arellano-jimenez, M., Peng, Z., Wang, T., Li, Y., Yakobson, B. I., Wei, S.-H., Yacaman, M. J., Tour, J. M. High-Performance Hydrogen Evolution from $MoS_{2(1-x)}P_x$ Solid Solution. *Adv. Mater.* **2016**, *28*, 1427−1432.

(71) Li, Q.; Han, C.; Ma, X.; Wang, D.; Xing, Z.; Yang, X. Bromine and Nitrogen Co-doped Tungsten Nanoarrays to Enable Hydrogen Evolution at all pH Values. *J. Mater. Chem. A* **2017**, *5*, 17856−17861.

(72) Hu, J.; Zhang, C.; Jiang, L.; Lin, H.; An, Y.; Zhou, D.; Leung, M. K. H.; Yang, S. Nanohybridization of MoS_2 with Layered Double Hydroxides Efficiently Synergizes the Hydrogen Evolution in Alkaline Media. *Joule* **2017**, *1*, 383−393.

(73) Chen, Y. Y.; Zhang, Y.; Zhang, X.; Tang, T.; Luo, H.; Niu, S.; Dai, Z. H.; Wan, L. J.; Hu, J. S. Self-Templated Fabrication of $MoNi_4/MoO_{3-x}$ Nanorod Arrays with Dual Active Components for Highly Efficient Hydrogen Evolution. *Adv. Mater.* **2017**, *29*, 1703311.

(74) Zhang, R.; Wang, X.; Yu, S.; Wen, T.; Zhu, X.; Yang, F.; Sun, X.; Wang, X.; Hu, W. Ternary $NiCo_2P_x$ Nanowires as pH-Universal Electrocatalysts for Highly Efficient Hydrogen Evolution Reaction. *Adv. Mater.* **2017**, *29*, 1605502.

(75) Tang, C.; Hu, Q.; Li, F.; He, C.; Chai, X.; Zhu, C.; Liu, J.; Zhang, Q.; Zhu, B.; Fan, L. Coupled Molybdenum Carbide and Nitride on Carbon Nanosheets: An Efficient and Durable Hydrogen Evolution Electrocatalyst in Both Acid and Alkaline Media. *Electrochim. Acta* **2018**, *280*, 323–331.
(76) Lv, Z.; Tahir, M.; Lang, X.; Yuan, G.; Pan, L.; Zhang, X.; Zou, J.-J. Well-Dispersed Molybdenum Nitrides on a Nitrogen-Doped Carbon Matrix for Highly Efficient Hydrogen Evolution in Alkaline Media. *J. Mater. Chem. A* **2017**, *5*, 20932–20937.
(77) Xiao, X., Huang, D., Fu, Y., Wen, M., Jiang, X., Lv, X., Li, M., Gao, L., Liu, S., Wang, M., Zhao, C., Shen, Y. Engineering NiS/Ni_2P Heterostructures for Efficient Electrocatalytic Water Splitting. *ACS Appl Mater Interfaces* **2018**, *10*, 4689–4696.
(78) Tsai, C.; Chan, K.; Nørskov, J. K.; Abildp-edersen, F. Theoretical Insights into the Hydrogen Evolution Activity of Layered Transition Metal Dichalcogenides. *Surf. Sci.* **2015**, *640*, 133–140.

FIGURES

Figure 1. (**a**) **Evolution of the different structures of MoS_2 and transmission electron microscope (TEM) observations of as-synthesized MoS_2.** Schematic representation of the multilayered molybdenum disulfide after the hydrothermal synthesis (blue), after annealing at 800 °C under Argon (green) and after annealing under H_2 below 600 °C (orange) and above 600 °C (red). The top and bottom MoS_2 structures represent the surface and the bulk sections of the MoS_2 nanosheets in the nanoflowers structures. The S vacancies are displayed in red circles. (**b**) TEM images of as-synthesized MoS_2. MoS_2 nanosheets organized in the form of nanoflowers. (**c, d**) High resolution TEM image of the stacked individual layers of as-synthesized MoS_2.

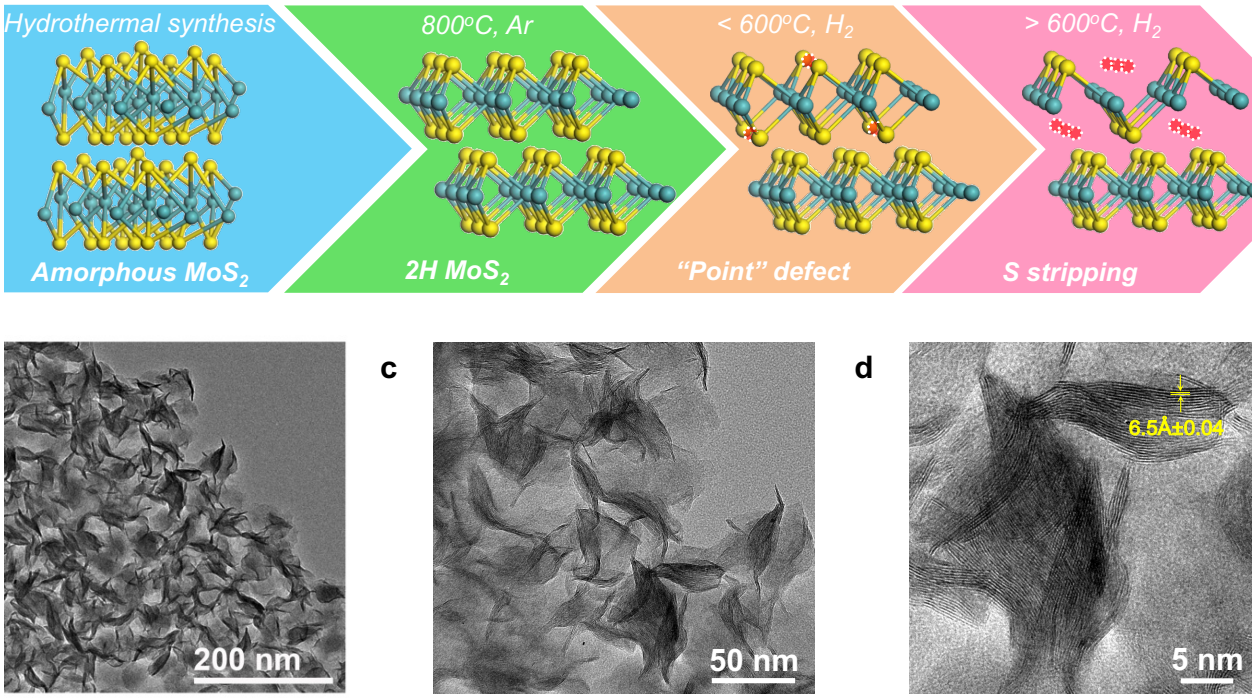

Figure 2. (**a, b**) **Transmission electron microscope observations of defected MoS_2.** Typical defects observed under high resolution TEM shows the creation of distortions and kinks in the slabs of MoS_2 due to disorder within the basal planes of the nanosheets. (**c**) High resolution TEM image of an ultra-thin layer of defected MoS_2-7H. The hexagonal symmetry of 2H MoS_2 can be identified. Examples of sulfur vacancies are highlighted by red cycles. (**d,i**) Elemental mapping of Mo and S from pristine (**d,e,f**) and defected (**g, h, i**) MoS_2 nanoflowers.

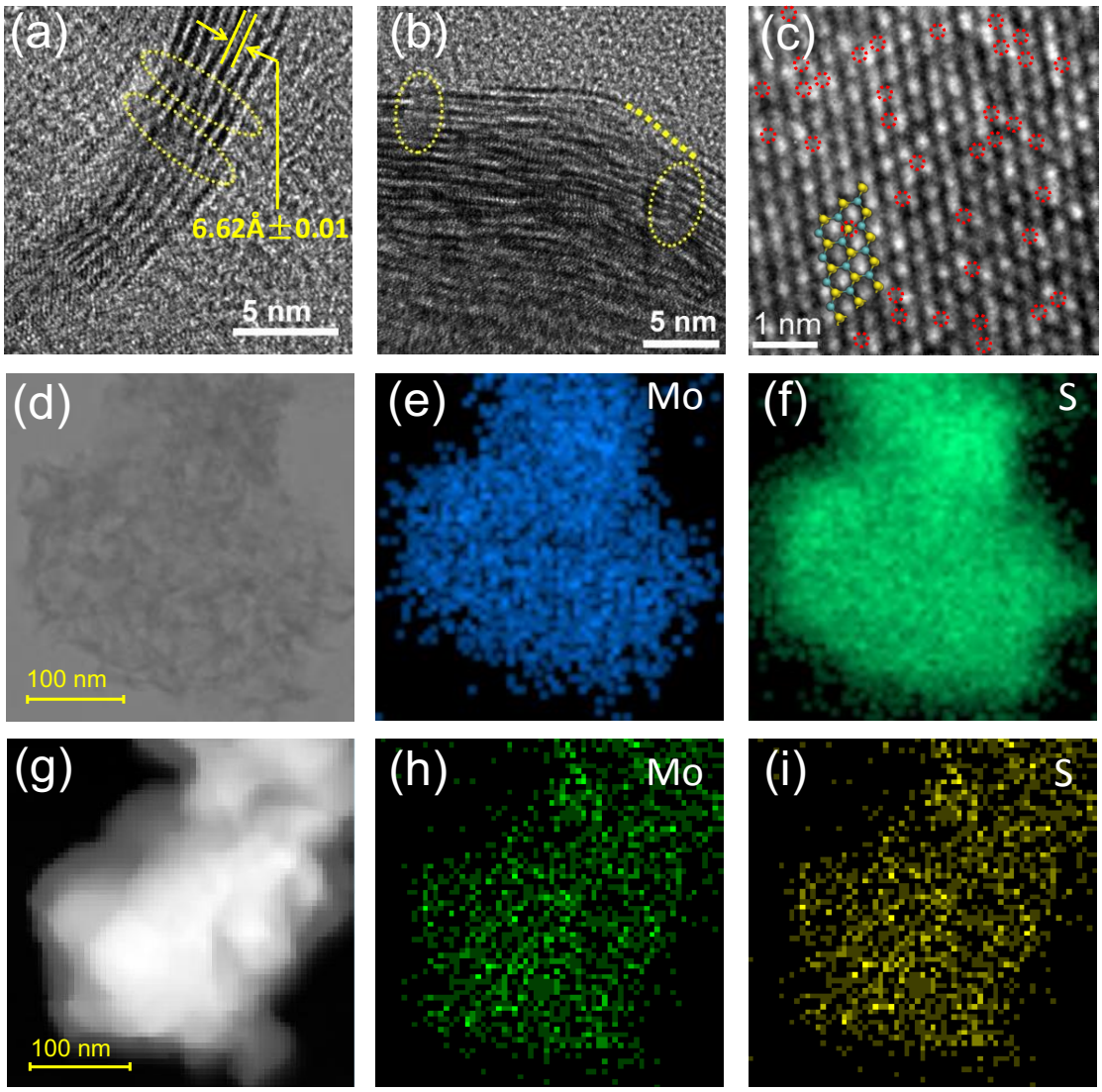

Figure 3. (**a**) **Characterizations of defected MoS_2 nanosheets.** Electron Paramagnetic Resonance (EPR) spectra generated by the Mo-S dangling bonds for the different defected MoS_2 compared to 2H MoS_2. Inset: Evolution of the intensity of the EPR signals as function of the annealing temperature. (**b**) High-resolution XPS spectra from the Mo3d and S2s regions for the 2H MoS_2 electrodes. The S2s signals (in green) vanish after 600 °C whereas the Mo(*UC*) doublets rapidly emerge because of the stripping of the S atoms from the MoS_2 slabs. (**c**) Evolution of the S:Mo and Mo(*UC*):Mo(VI) ratios as a function of the annealing temperature of the electrodes. The two domains of point defects and S stripping are shaded in orange and red

respectively. Inset: Evolution of the Mo(*UC*):Mo(IV) as a function of the S:Mo ratio. (**d**) Turnover frequency (TOF) from amorphous and 2H MoS_2 at pH≈0 and pH≈13. 2H MoS_2 performs the same at both pH values, while the activity from amorphous MoS_2 is strongly reduced at pH≈13.

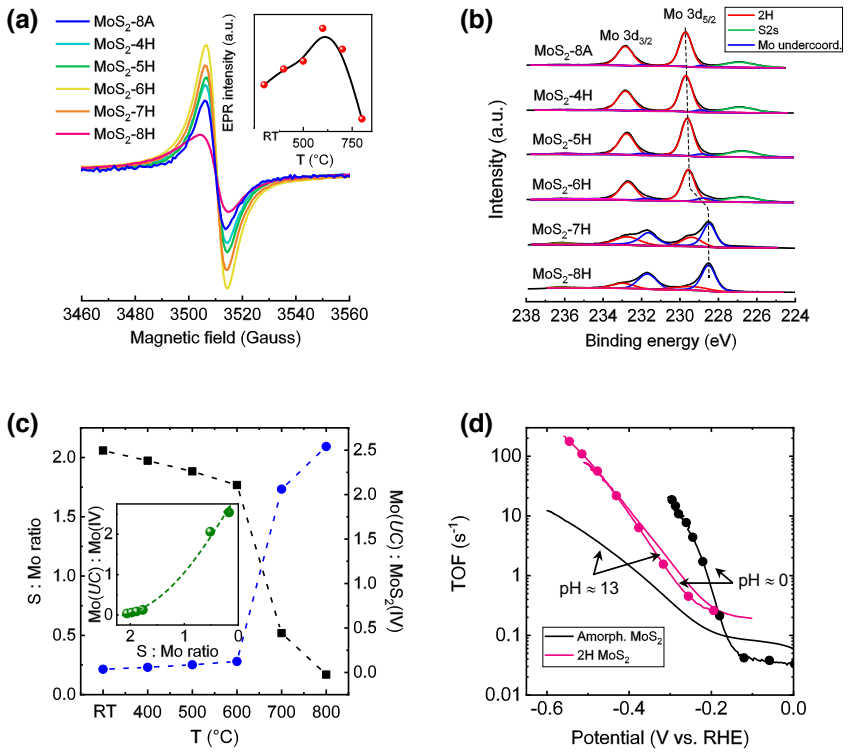

Figure 4. (a,b) Electrocatalysis measurements towards hydrogen evolution from defected MoS_2 nanosheets. Polarization curves of 2H MoS_2 and defected 2H MoS_2 after annealing from 400 °C up to 800 °C under H_2. There are identical legends for figures (**a**), (**b**), (**d**) and (**e**). (**c**) Evolution of the Tafel slopes with the annealing temperatures and measured at pH≈0 and pH≈13. (**d,e**) Evolution of the TOF with the applied potential for the defected MoS_2 electrodes. (**f**) Evolution of the TOF measured at 300 mV overpotential for 2H MoS_2 and MoS_2-*x*H and

measured at pH≈0 and pH≈13. The repaired 2H-MoS_2 electrode (MoS_2-7S) is also presented to confirm the healing function.

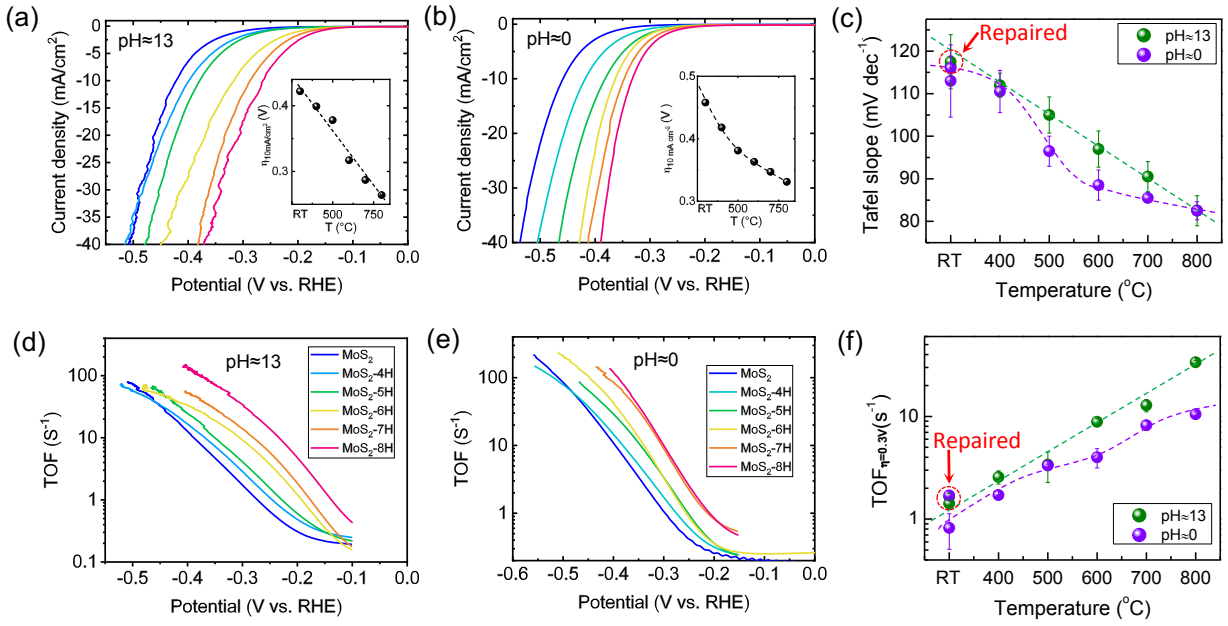

Figure 5. (**a**) **Turnover frequency (TOF) from defected MoS_2 nanosheets.** Evolution of the overpotential for reaching TOF = 2 s^{-1} with the S:Mo ratio measured by XPS. (**b,c**) Evolution of the TOF at 300 mV with the S:Mo ratio and measured at pH≈0 and pH≈13. The repaired 2H-MoS_2 electrode (MoS_2-7S) is also presented and shows similar performance as pristine 2H MoS_2 (MoS_2-8A).

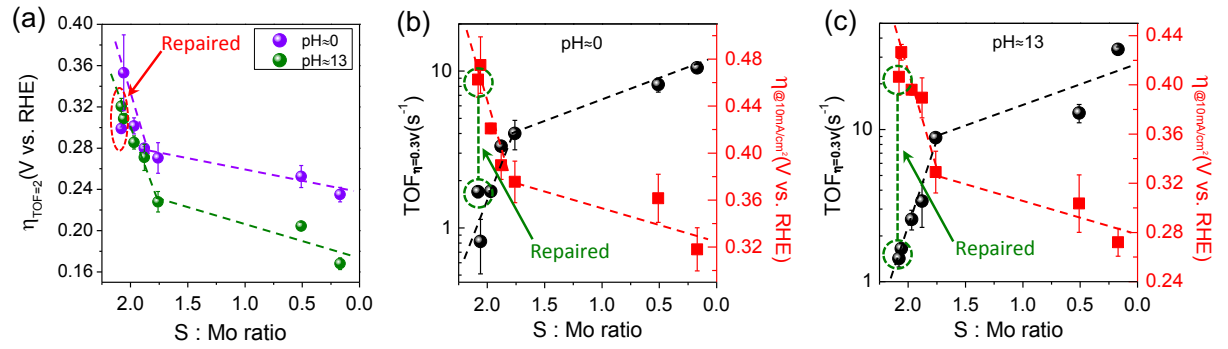

Figure 6. Comparison of the HER activity with other electrocatalysts. Evolution of the TOF at pH≈0 (**a**, 0.5 M H_2SO_4) and pH≈13 (**b**, 0.1 M KOH) from amorphous and MoS_2-7H compared to values from the state of the art HER electrocatalysts (pH≈0: P-1T MoS_2,[55] MoS_2/Mo_2C,[57] hH-MoS_2,[65] Stepped MoS_2,[67] $MoS_{2(1-x)}Se_{2x}/NiSe_2$,[68] MoP|S,[69] $MoS_{2(1-x)}P_x$,[70] W/BrN;[71] pH≈13: MoS_2/NiCo-LDH,[72] $MoNi_4/MoO_{3-x}$,[73] $NiCo_2P_x$,[74] Mo_2C/Mo_2N,[75] Mo_2N@NC,[76] NiS/Ni_2P/CC[77]).